Journal of Materials Chemistry A

ROYAL SOCIETY OF CHEMISTRY

PAPER

View Article Online
View Journal | View Issue



Cite this: J. Mater. Chem. A, 2026, 14, 23457

# A bismuth ferrite-based lead-free piezoelectric ceramic surpassing PZT-8 in thermal stability

Xiaodong Yan,[a] Chaoyang Shi,[b] Jianjun Wu,[c] Kevin Chen*[d] and Zhengbao Yang *[a]

Piezoelectric materials are essential for electronics but suffer from thermal instability, especially lead-free alternatives to lead zirconate titanate (PZT). The absence of quantitative thermal stability metrics has hindered progress. In this work, we introduce a new index, denoted as "$S_d$", which accounts for both the operating temperature range and the central operating temperature, allowing for a comprehensive assessment. Applying this criterion, we found that the commercial PZT-4 material exhibits the highest thermal stability among the ceramics tested, confirming its reputation as the industry standard. Notably, we developed a new lead-free piezoelectric ceramic based on bismuth ferrite that achieved a stable piezoelectric coefficient at 38–247 °C; the corresponding $S_d$ value (173) exceeds that (163) of commercial PZT-8 (20–232 °C). Further analysis revealed that reducing the concentration of point defects improved its electrical homogeneity and reduced conductivity, leading to enhanced thermal stability. This work provides a new evaluation framework that can accelerate the development of thermally stable lead-free piezoelectric materials. The implications of this research extend beyond piezoelectrics, as the $S_d$ index could find broader application in the characterization of other functional oxides.

Received 27th November 2025
Accepted 17th April 2026

DOI: 10.1039/d5ta09690a

rsc.li/materials-a



## 1. Introduction

Piezoelectric materials can achieve mutual conversion between mechanical energy and electrical energy and are key components in sensors, transducers, and actuators.[1–3] With the increasing requirement for piezoelectric devices in extreme environments, such as aerospace and deep petroleum exploration,[4] large piezoelectricity with good temperature stability has become an urgent need. Due to its excellent performance,[5–7] PZT dominates the market for more than half a century. Unfortunately, PZT is now facing worldwide legislative restrictions due to its toxicity, and this has triggered a worldwide search for Pb-free substitutes.[7–12]

Currently, the main lead-free piezoelectric materials include $BaTiO_3$ (BT)-based, (K, Na)$NbO_3$ (KNN)-based, $(Na_{0.5}Bi_{0.5})TiO_3$ (NBT)-based and $BiFeO_3$ (BF)-based perovskite systems. Among them, the $BiFeO_3$-based ferroelectrics, such as bismuth ferrite–barium titanate ($BiFeO_3$–$BaTiO_3$, BF–BT), possess high Curie temperature and strong spontaneous polarization,[13–17] making them potential alternatives to lead-containing piezoelectrics. However, high dielectric loss and high conductivity severely hinder the stability of their piezoelectric properties.[13,15] It was reported that the small-signal piezoelectric coefficient presents a large fluctuation (as high as 50% from 25 °C to 150 °C),[18] and the large-signal piezoelectric coefficient remains stable below 150 °C or even lower due to leakage.[19–21]

In addition, there is no international standard to evaluate the temperature stability of piezoelectricity. By referring to the evaluation method of the stability of capacitors,[22–24] we know that the temperature coefficient of piezoelectricity (TCP) can be defined usually by the formula as follow:

$$\mathrm{TCP} = \frac{\Delta d_{33}}{d_{33,b}} = \frac{d_{33,T} - d_{33,b}}{d_{33,b}} \quad (1)$$

where $d_{33,T}$ is the piezoelectric coefficient at any temperature $T$, and $d_{33,b}$ is the piezoelectric coefficient at the benchmark temperature. Researchers usually set room temperature as the benchmark temperature. For high temperature applications, materials need to work at 200 °C or even 300 °C; therefore, it is unreasonable to use 25 °C as the benchmark. Following the international standard for capacitance,[22,24] the values of TCP $\leq \pm 15\%$ were considered to be the temperature-stable range; however, it is not completely applicable to the piezoelectric coefficient because of the permanent decay of piezoelectricity at the temperature where $d_{33}$ reaches its last peak (usually at the de-polarization temperature, $T_d$). Here, the low and high temperature boundaries determined by TCP conditions are denoted as $T_l$ and $T_h$, respectively. As shown in Fig. 1a, for case one, $T_d$ is higher than $T_h$; the eventual stable range is consistent

[a]Department of Mechanical and Aerospace Engineering, The Hong Kong University of Science and Technology, Clear Water Bay, Hong Kong, China. E-mail: zbyang@ust.hk
[b]School of Mechanical Engineering, Tianjin University, Tianjin 300072, China
[c]Sichuan Energy Investment Tianfu Clean Energy Research Institute, Chengdu 610041, China
[d]Department of Electronic and Computer Engineering, The Hong Kong University of Science and Technology, Clear Water Bay, Hong Kong, China. E-mail: eekjchen@ust.hk

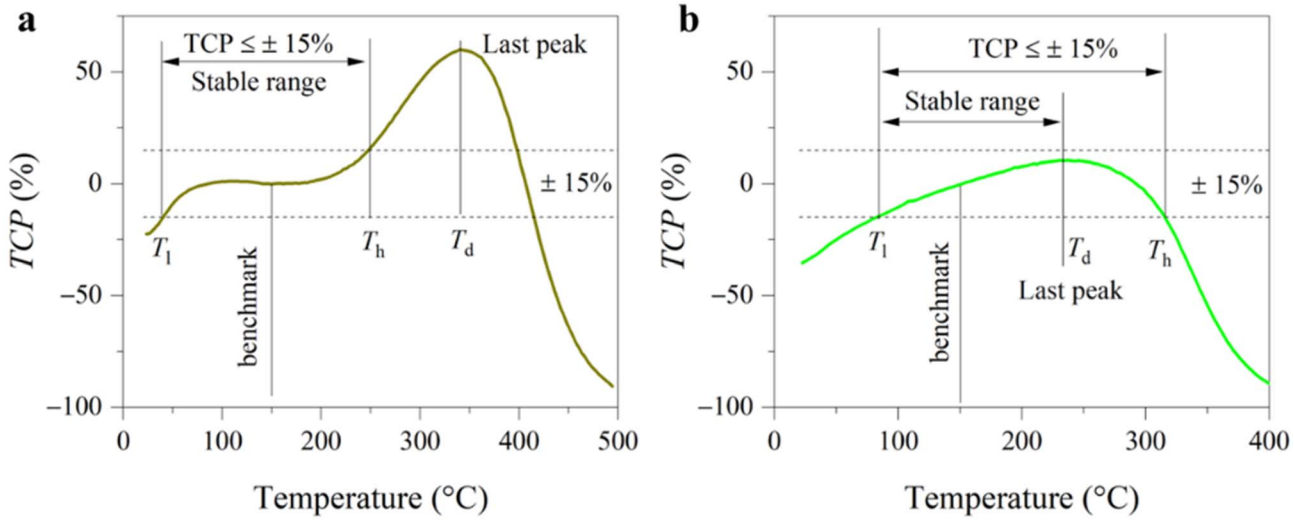


Fig. 1 Determination of the temperature-stable range. To simplify, the low and high temperature boundaries determined by TCP conditions are named $T_l$ and $T_h$. (a) For case one, since the temperature where the last peak occurs ($T_d$) is higher than $T_h$, the upper limit temperature ($T_{max}$) of the stable range is equal to $T_h$. (b) For case two, $T_d$ is lower than $T_h$; therefore, $T_{max}$ is equal to $T_d$. As a result, $T_{max}$ should be taken as the smaller of $T_h$ and $T_d$.

with that determined by TCP conditions. But for case two (Fig. 1b), $T_d$ is much lower than $T_h$; therefore, the upper limit temperature of the stable range is equal to $T_d$ rather than $T_h$. Unfortunately, the researchers seldom discuss and even ignore this difference,[4,25,26] which severely limits the development of high temperature piezoelectric materials.

Here, based on the redefinition of the temperature-stable range, we propose a new criterion for evaluating the stability of piezoelectricity. Specifically, this criterion emphasizes that both high operating temperature and wide temperature range are crucial for temperature-stability (a new stability index) of piezoelectric coefficient $d_{33}$. We calculated the index value of different piezoceramics and found that the highest value of up to 224 belongs to PZT-4, a well-known piezoceramic with the widest temperature range and high operating temperature. In contrast, within the lead-free piezoceramic category, we did not identify any materials that match the performance of their lead-based counterparts. To address this gap, we designed a new lead-free ceramic (Sm doped $0.7BiFeO_3$–$0.3BaTiO_3$, composition near the morphotropic phase boundary[15]) with an index value of 173 (temperature-stable range of 38–247 °C), much higher than that of its undoped counterpart (152), and even comparable to that (163) of PZT-8 (20–232 °C). We further analyzed the origins of the temperature-stable piezoelectricity in the doped $BiFeO_3$–$BaTiO_3$ ceramics. Our results indicate that a significantly reduced concentration of point defects enhances electrical homogeneity and decreases conductivity, contributing to improved thermal stability.

## 2. Results and discussion

### 2.1 The new metric of temperature stability of piezoelectricity

We first selected classical materials including commercial PZTs and lead-free ones to verify reliability. Fig. 2a shows the piezoelectric coefficients of BF–BT, Sm-doped BF–BT, (Ba, Ca) (Ti, Zr)$O_3$ (BCTZ)[27] and commercial PZTs at various temperatures. For the BCTZ ceramic, $d_{33}$ is approximately 500 pC $N^{-1}$ at room temperature, but it is extremely sensitive to temperature due to low Curie temperature and polymorphic phase transition.[28,29] For the PZT family, their piezoelectric coefficients show no obvious decay up to nearly 300 °C. Among them, PZT-5A, a soft piezoelectric material, shows the highest $d_{33}$ value and a large fluctuation with temperature. In comparison, hard PZTs (PZT-4 and PZT-8) show more stable $d_{33}$ values. Interestingly, although the $d_{33}$ value of Sm-BF–BT at room temperature is slightly lower than that of hard PZT-8, it is more resistant to high temperatures. We calculate the temperature coefficient of piezoelectricity (TCP) according to formula (1). In view that the high temperature piezoelectric devices need to work at 300 °C or above,[4] the benchmark temperature was set to 150 °C. Therefore, the temperature-stable range of the piezoelectric coefficient is identified preliminary based on TCP ≤ ±15%,[22] as shown in Fig. 2b. Apart from the TCP conditions, we considered the permanent decay of the piezoelectric coefficient at de-polarization temperature ($T_d$). For PZT-4, PZT-5A and BF–BT, because $T_d$ is lower than the high temperature boundary ($T_h$) determined by TCP conditions, the former is determined as the upper limit temperature ($T_{max}$) of the temperature-stable range. Fig. 2c shows the stable range of $d_{33}$ of lead-free BF–BT, Sm-BF–BT and PZTs. It can be found that PZT-4 has the widest temperature range (20–318 °C). PZT-8 (20–232 °C) is more stable than PZT-5A (86–314 °C) at below 200 °C, but it is inferior to the latter at higher temperature, even not as stable as lead-free Sm-BF–BT (38–247 °C). Obviously, this comparison is still not intuitive enough.

To quantify this difference, we propose a new index to evaluate the stability of piezoelectric coefficient $d_{33}$ ($S_d$) as follows:

$$S_d = \sqrt{\Delta T \times T_{center}} = \sqrt{(T_{max} - T_{min}) \times \frac{T_{max} + T_{min}}{2}} \quad (2)$$

 

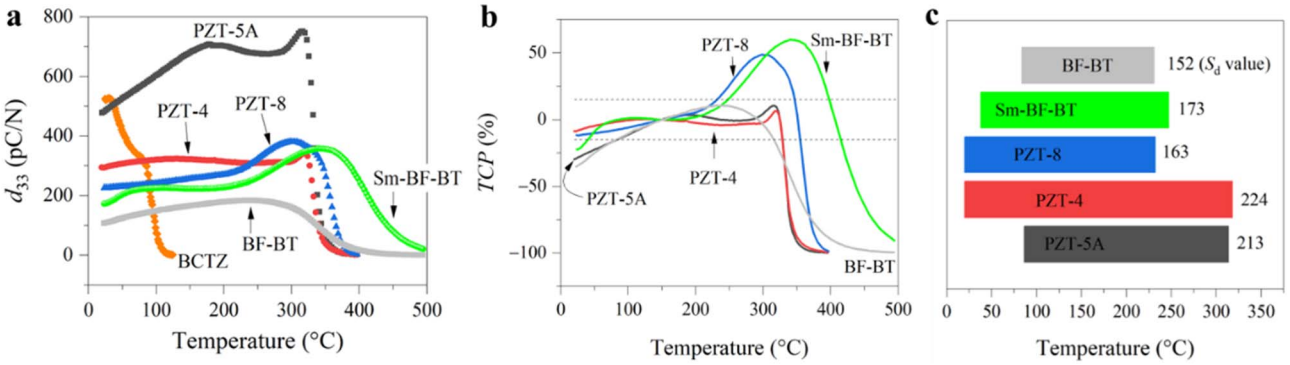


Fig. 2 The evaluation of temperature stability of piezoelectricity. (a) The piezoelectric coefficient $d_{33}$ of lead-free BCTZ, BF–BT, Sm-doped BF–BT and commercial PZTs. (b) The temperature coefficient. (c) The temperature-stable range and thermal stability metric $S_d$ of $d_{33}$ of lead-free Sm-doped BF–BT and commercial PZTs based on a benchmark of 150 °C.

where $T_{max}$ and $T_{min}$ are the upper and lower limit temperatures in the temperature range of stable $d_{33}$. Formula (2) is valid and applicable only when the temperature is above zero. A large $\Delta T$ means a wide temperature range, and high $T_{center}$ means a high operating temperature. The importance of $\Delta T$ is obvious; $T_{center}$ is also essential because the piezoelectric materials usually suffer from de-polarization problems when temperature increases. As the stability of piezoelectric coefficient $d_{33}$ is closely related to temperature (including phase transition temperature and Curie temperature), we take the square root of the product of $\Delta T$ and $T_{center}$ as $S_d$, which will make its unit consistent with the temperature. Although the index $S_d$ has no specific physical meaning, it is deduced by combining the evaluation criteria for temperature stability of capacitors and de-polarization of piezoelectric materials and is more practical for judging temperature stability among various material systems. The higher the $S_d$ value is, the better the temperature stability is. For ferroelectric materials, the piezoelectric properties are only suppressed at low temperatures due to weakened domain wall motion, while they will suffer permanent degradation at high temperatures. Therefore, the stability at high temperature (above room temperature) was paid more attention.

According to formula (2), we calculated the $S_d$ value of lead-free BF–BT, Sm-BF–BT and PZTs, as marked in Fig. 2c. The highest $S_d$ value was obtained in PZT-4, thanks to its wide temperature range and high upper limit temperature, which is consistent with previous cognition that PZT-4 is one of the most stable piezoelectric materials.[30] Due to a low upper-limit temperature, the $S_d$ value of PZT-8 is much lower than those of PZT-4 and PZT-5A. In addition, we find that the $S_d$ value (173) of Sm doped BF–BT (temperature range of 38–247 °C) is higher than that (152) of its undoped counterpart, and even comparable to that (163) of PZT-8 (temperature range of 20–232 °C). We further check the influence of the threshold (Fig. S1) and benchmark temperature (Fig. S2) on the temperature-stable range and $S_d$ value. The results indicate that only slight differences arise when the benchmark temperature is changed to 100

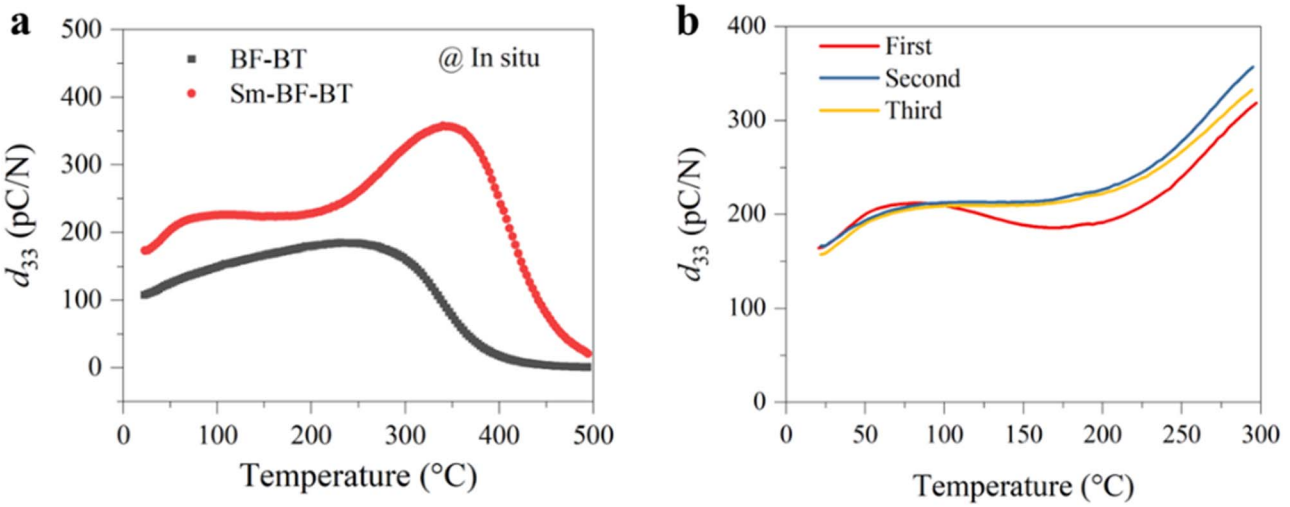


Fig. 3 Piezoelectricity of lead-free BF–BT ceramics at various temperatures. (a) The piezoelectric coefficient $d_{33}$ of BF–BT and Sm doped BF–BT ceramics at 20–500 °C. (b) $d_{33}$ of Sm doped BF–BT ceramics under first, second and third heating cycles from 20 to 300 °C.

°C. In other cases, the prerequisites have no significant influence on the comparative results of $S_d$.

### 2.2 The enhanced and temperature-stable piezoelectricity in Sm-doped BF–BT ceramics

We next investigate the piezoelectricity and its temperature stability of the Sm-doped BF–BT ceramic. Here, the optimal doping content was determined through a preliminary experiment, in which $0.7BiFeO_3$–$0.3Ba_{1-x}Sm_xTiO_3$ ($x$ from 0.00 to 0.04) ceramics were prepared and electrical properties were measured (Fig. S3). The result shows that $0.7BiFeO_3$–$0.3Ba_{0.99}Sm_{0.01}TiO_3$ has the highest $d_{33}$ value and dielectric permittivity at room temperature. Fig. 3a shows piezoelectric coefficients of undoped and Sm-doped BF–BT ceramics at various temperatures. On the one hand, at room temperature, $d_{33}$ of the doped sample is about 175 pC $N^{-1}$, which is much higher than that of its undoped counterpart. On the other hand, the $d_{33}$ of the undoped sample starts to fall once the temperature approaches 230 °C; in comparison, $d_{33}$ of the doped one shows no obvious decay until the temperature is near 340 °C, indicating better thermal stability. We further assess the reliability of piezoelectricity of the Sm-BF–BT ceramic. $d_{33}$ of the poled sample is measured three times during the heating process from 20 to 300 °C, as shown in Fig. 3b. In the measurement, the sample was cooled to 20 °C before the next test starts. We can see that $d_{33}$ under the second heating presents a small difference compared to that under the first measurement, and there is almost no difference between the third and second measurements, particularly in the temperature below 200 °C. These results suggest that the Sm-doped BF–BT ceramic has a good thermal cycling stability.

We not only improved the piezoelectricity at room temperature but also enhanced the temperature stability by doping. First, we explored the mechanism behind the improvement of piezoelectric properties. Fig. 4a shows the polarization–electric field ($P$–$E$) hysteresis loop of the poled samples. After doping, the $P$–$E$ loop shrinks, accompanied by a decrease in coercive field and remnant polarization, but it still exhibits a high remnant polarization of 34 μC $cm^{-2}$. Fig. 4b shows their strain–electric field ($S$–$E$) loops. The asymmetric shape is because the sample was pre-poled with a DC field before the measurement, causing the alignment of defect dipoles.[5,21] It is noted that the direction of defect dipoles is unchanged after the first electric

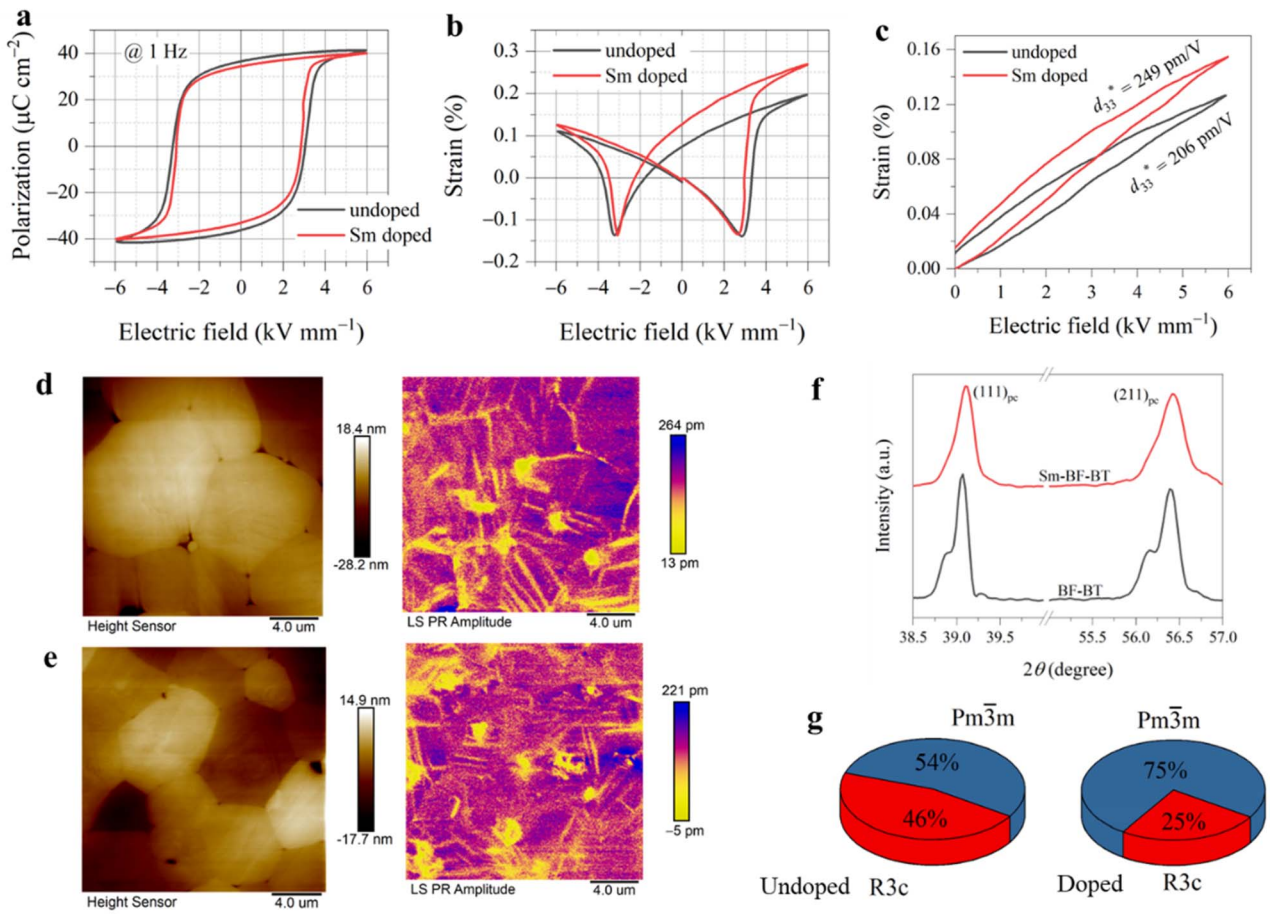


Fig. 4 The electrical properties and microstructure at room temperature. The polarization (a) and strain (b) of undoped and Sm-doped samples under the bipolar electric field at 1 Hz. (c) The unipolar strain at 1 Hz. The surface topography and piezoelectric amplitude images of the undoped (d) and Sm-doped (e) samples observed using a piezoresponse force microscope. (f) The X-ray diffraction patterns. (g) The phase content obtained by Rietveld refinement.

 

treatment, but they can be stretched or contracted. The amplitude of strain is determined by the behaviors of defect dipoles and spontaneous polarization.[5] The larger strain under the positive electric field is due to the initially applied electric field being the same as the polarization direction of the sample. In this case, the defect dipoles are stretched and spontaneous polarization is aligned along the applied field. Under the negative electric field, the defect dipoles are contracted and spontaneous polarization is also aligned along the applied field. Despite that, the *P*–*E* loop is almost symmetric because the effect of defect dipoles and spontaneous polarization on measured polarization is the same regardless of the direction of the applied electric field.[5] From Fig. 4b, we can also observe a decrease in coercive field and a significant increase in strain for the doped sample. We further measured the strain under a unipolar electric field. As shown in Fig. 4c, the doped sample exhibited a larger unipolar strain, corresponding to an increase in the piezoelectric strain coefficient from 206 to 249 pm $V^{-1}$. The macroscopic electrical properties are closely related to the microstructure and domain structure of the crystals.[2,31] We observed the domain structure of the samples using piezoresponse force microscopy, as shown in Fig. 4d and e. Both samples exhibited clear ferroelectric domain morphology, and regular lamellar/strip domains dominate.[32] Interestingly, the domain size significantly decreased, and the domain density increased after doping. This may be related to the reduced grain size (Fig. 4e and S4) and altered crystal structure.[33,34]

Fig. 4f and S5 show the X-ray diffraction patterns of the samples. Both undoped and doped samples exhibit a pure perovskite phase. After doping, the diffraction peaks shift towards higher angles, indicating a decrease in lattice volume. This is due to the fact that $Sm^{3+}$ (1.24 Å) has a smaller radius compared to $Ba^{2+}$ (1.61 Å).[35] Additionally, it can be observed that the split diffraction peaks become less pronounced after doping. It has been reported that 0.7BF–0.3BT exhibits a crystal structure with coexisting rhombohedral *R*3*c* and pseudo-cubic *Pm*$\bar{3}$*m* phases.[36,37] We performed fitting of the patterns using a mixed-phase of *R*3*c* and *Pm*$\bar{3}$*m*. It can be observed that the content of the *R*3*c* phase significantly decreases after doping (Fig. 4g and Table S1), indicating an enhanced symmetry of the crystal structure. Previous reports have indicated that differences in valence and ionic radii lead to discontinuities in the crystal structure and polarization,[2] increasing the interfacial energy of the system. Competition between the bulk and interfacial energy may lead to a flattened free-energy profile,[38] consistent with the enhanced symmetry of the crystal structure and reduced domain size. In addition, the higher electronegativity of $Sm^{3+}$ compared to $Ba^{2+}$ increases the degree of local covalent bonding, and the hybridization of ionic and covalent bonds can also promote piezoelectricity.[11]

Second, we investigate the origin of enhanced thermal stability. It is well known that the Curie temperature of a ferroelectric is a critical factor affecting the stability of piezoelectricity.[30] Fig. 5a and S6 present the temperature-dependent dielectric permittivity and loss of undoped and doped BF–BT ceramics. We can see that the undoped sample presents a high Curie temperature of ~510 °C. After doping, the Curie temperature decreases to ~490 °C. Generally, a higher Curie temperature corresponds to a higher thermal depolarization temperature and thus greater stability of the piezoelectric performance.[30] However, in our work, the doped sample exhibits the higher operating temperature and enhanced piezoelectric stability (Fig. 3a). First, the temperature stability of electrical properties depends on the lattice symmetry. A ferroelectric with low lattice symmetry presents a large fluctuation with the temperature due to the fragmentation of long-range ferroelectric order. For ferroelectrics with high symmetry, the change is usually smooth.[39] In BFO-based systems, there were multiple phase transitions from room temperature to the Curie temperature.[40] After doping, the lattice symmetry increases, and phase transition becomes less abrupt; thus, the stability of dielectric permittivity and piezoelectricity is highly improved. As shown in Fig. S6, we can find that a small hump near 300 °C disappeared after Sm doping. Second, the point defect, such as oxygen vacancies, is also a vital factor that affects the temperature stability. By comparing the dielectric permittivity and loss at a lower temperature range (Fig. 5b and c), we can see that the undoped sample exhibits extremely unstable dielectric properties, particularly in terms of dielectric loss, where an obvious rise occurs at temperatures near 100 °C. Dielectric loss originates from electrically active regions such as point defects.[41] For BF-based materials, bismuth volatilization, reduction of iron ions, and self-decomposition of BF can lead to the generation of oxygen vacancies.[42] In contrast, the doped sample shows

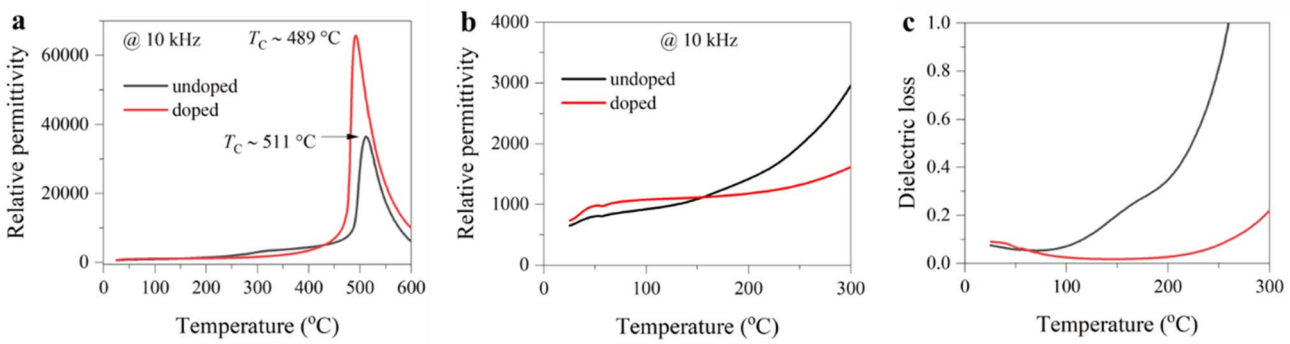


Fig. 5 The dielectric properties of BF–BT samples. (a) The temperature-dependent dielectric permittivity at 10 kHz. (b and c) The dielectric permittivity (b) and loss (c) from 20 °C to 300 °C, showing more stable dielectric properties after Sm doping.

significantly enhanced stability in dielectric properties, with a dielectric loss below 0.1 in the temperature range from room temperature to 250 °C.

To further identify the point defects, we measured the impedance spectra of the samples at elevated temperatures. Fig. 6a displays the impedance complex plane plots of the undoped sample. Interestingly, we observe two semicircular arcs, indicating that the impedance of the sample is composed of two different electrical responses,[43] namely grain and grain boundary, in the order of decreasing frequency. In contrast, in the doped sample, only a single arc can be observed in this temperature range, as shown in Fig. 6b. This electrical response implies that the resistance of grains in the doped sample is much larger than that in the undoped sample; therefore, the resistance of grains and grain boundaries becomes comparable. Previous reports pointed out the presence of a core–shell microstructure in BF–BT-based ceramics,[44] consisting of an electrically active core and a resistive shell. As shown in Fig. S7, we can observe dark shells and bright cores within individual grains, representing Ba, Ti rich and Bi, Fe rich regions, respectively. The electrically active cores may be attributed to an abundance of defects.[44] Additionally, we find that the resistance (the intersection points of the arc and the X-axis) of the doped sample increases by an order of magnitude than its undoped counterpart at the same temperature. To further understand the defect dynamics, quantitative analysis was conducted. The measured impedance spectra were fitted according to an equivalent circuit. For the undoped sample, a circuit consisting of two parallel resistance ($R$) and constant phase ($Q$) elements connected in series (Fig. S8) was adopted,[45] while only a parallel $R$ and $Q$ element was required in the doped sample due to the single arc. The fitted curves are displayed in Fig. S9. Based on

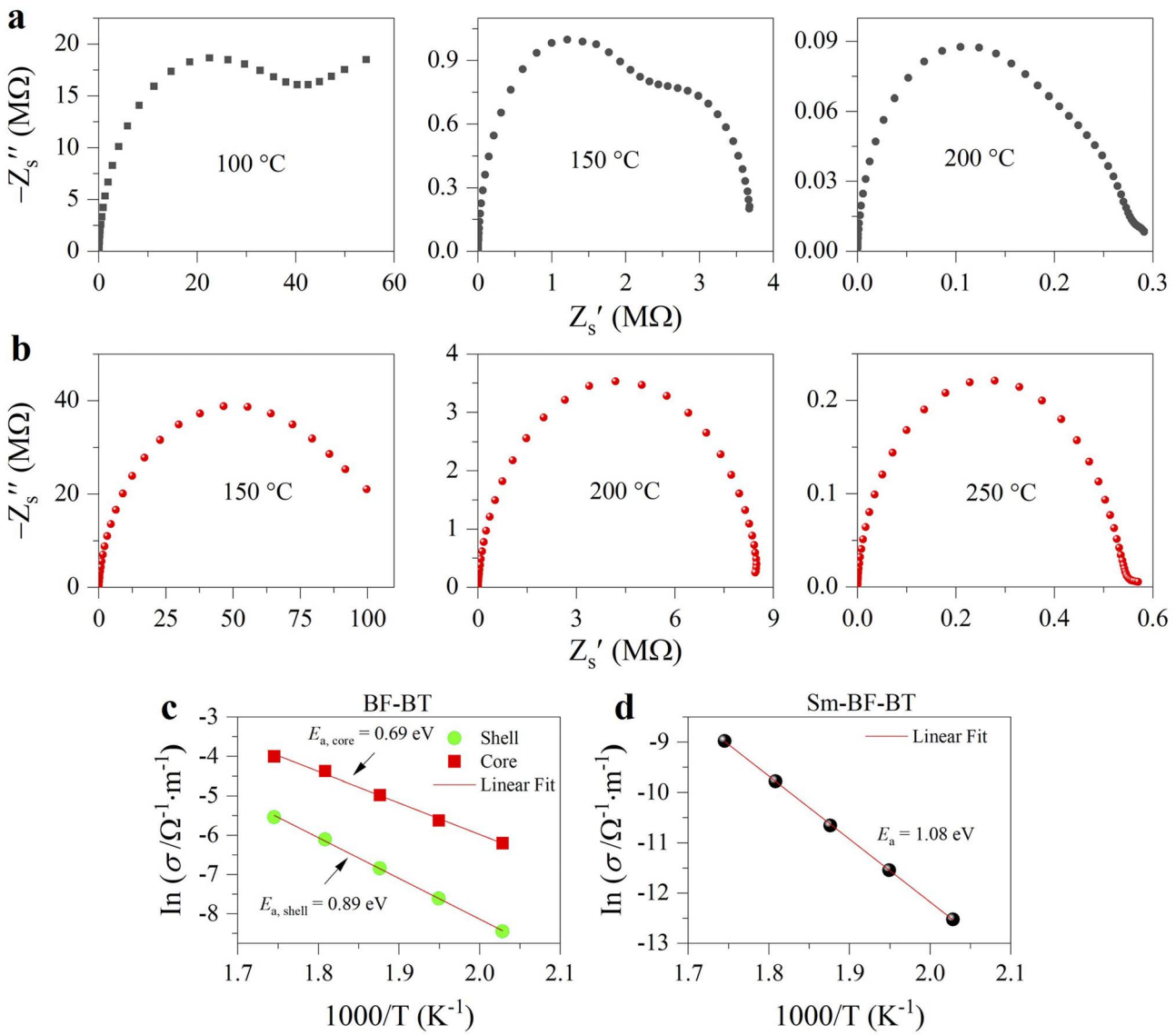


Fig. 6 The high-temperature impedance and defect chemistry analysis. Impedance complex plane plots for the undoped (a) and doped (b) samples at various temperatures. (c) Core and shell conductivities of the BF–BT ceramic. (d) Bulk conductivity of the Sm-doped BF–BT ceramic. The solid line is a result of linear least-square fitting.

 

a previous report,[45] the temperature dependence of the conductivities of undoped and doped ceramics was calculated and is presented in Fig. 6c and d. The conductivities of two specimens roughly show an Arrhenius-type behavior.[46,47] It can be observed that the conductivity of the Sm doped sample is significantly lower than that of the undoped sample (core and shell). Moreover, corresponding activation energies ($E_a$) derived from the Arrhenius equation[46] are given in Fig. 6c and d. For the undoped sample, core and shell activation energies are 0.69 eV and 0.89 eV, respectively. In comparison, the activation energy (1.08 eV) for the Sm doped sample is much higher than those of the undoped ones. The increased $E_a$ further proves a decrease in oxygen vacancy concentration.[48]

In the BF-based system, both the reduction of $Fe^{3+}$ and volatilization of $Bi^{3+}$ lead to a decrease in positive charge.[42] To maintain the electrical neutrality, extra oxygen vacancies are generated. The defect chemistry can be represented as follows:

$$2BiFeO_3 \rightarrow 2Fe_{Fe}^{\times} + 3O_O^{\times} + 2V_{Bi}^{'''} + 3V_O^{\cdot\cdot} + Bi_2O_3\uparrow$$

$$4BiFeO_3 \rightarrow 4Bi_{Bi}^{\times} + 10O_O^{\times} + 4Fe_{Fe^{3+}}^{2+'} + 2V_O^{\cdot\cdot} + O_2\uparrow$$

These oxygen and cation vacancies are coupled to form defect dipoles, which increase the conductivity of the ceramic and generate leakage currents, especially at high temperatures or under strong electric fields. With the introduction of $Sm^{3+}$ ions at the Ba site, compensating positive charges mitigate the generation of oxygen vacancies, as shown in the following formula:[42]w

$$2Sm_2O_3 \xrightarrow{Ba^{2+}} 4Sm_{Ba}^{\cdot} + 8O_O^{\times} - 2V_O^{\cdot\cdot} - O_2\uparrow$$

here the symbol "−" represents the decrease. The extra positive charges due to the $Sm^{3+}$ substitution in the Ba site lead to a decreased concentration of oxygen vacancies. To provide direct experimental evidence, the X-ray photoelectron spectroscopy (XPS) test was conducted on the undoped and doped ceramic powders, as shown in Fig. S10. The splitting of the O 1s signals observed in the XPS spectra indicates the presence of oxygen vacancies. It was found that the shoulder peak became less obvious after Sm doping. Furthermore, the quantification analysis of the elements shows that the relative content of oxygen in the doped sample (52%) is higher than that in the undoped one (48%), implying a decrease in oxygen vacancy concentration.

After Sm doping, the main defect dipoles $V_{Bi}^{'''} - V_O^{\cdot\cdot}$ and $Fe_{Fe^{3+}}^{2+'} - V_O^{\cdot\cdot}$ in the perovskite $ABO_3$ structure were changed to $V_{Bi}^{'''} - Sm_{Ba}^{\cdot}$ and $Fe_{Fe^{3+}}^{2+'} - Sm_{Ba}^{\cdot}$. Among them, $V_{Bi}^{'''} - V_{Bi}^{\cdot\cdot}$ and $Fe_{Fe^{3+}}^{2+'} - V_O^{\cdot\cdot}$ are along the ⟨110⟩ and ⟨001⟩ directions,[49] and the defect dipole reorientation needs only 1 step of $V_O^{\cdot\cdot}$ migration.[5] In comparison, both $V_{Bi}^{'''} - Sm_{Ba}^{\cdot}$ and $Fe_{Fe^{3+}}^{2+'} - Sm_{Ba}^{\cdot}$ are along the ⟨111⟩ direction, which is consistent with the directions of ferroelectric polarization in the rhombohedral phase.[3] $Fe_{Fe^{3+}}^{2+'} - Sm_{Ba}^{\cdot}$ cannot move due to the absence of ion exchange channels, and the $V_{Bi}^{'''}$ in defect dipole $V_{Bi}^{'''} - Sm_{Ba}^{\cdot}$ needs 2 steps of migration to realize reorientation, thus costing much more energy. Therefore, it is more difficult for Sm-doped BF–BT to depolarize, which will contribute to improved thermal stability at high temperature.

To investigate the impact of electrical homogeneity on the poling process and piezoelectric properties, we developed two physical models (Fig. S11 and Table S2). The first model consists of a conducting core and an insulating shell, simulating the undoped sample, while the second model features a core with conductivity similar to that of the shell, representing the doped sample. Using COMSOL 6.1 (Physics of current), we analyzed the polarization distribution (Fig. 7). Our results show that in electrically inhomogeneous dielectrics, the conducting core exhibits minimal polarization (Fig. 7a), as the electric field is primarily concentrated in regions with higher resistivity (Fig. S11). In contrast, electrically homogeneous dielectrics display more uniform polarization distribution in entire regions (Fig. 7b). Furthermore, the high-temperature ferroelectric measurements support these findings. As shown in Fig. S12, the undoped sample begins to exhibit leakage at 50 °C, whereas the doped sample remains stable until 150 °C. The significant leakage in the undoped sample leads to insufficient alignment of ferroelectric domains, which is reflected in the impedance and phase spectrum at the resonance frequency (Fig. S13).[50] Notably, the maximum phase angle of the doped sample is significantly higher than that of the undoped sample. Our results clearly demonstrate that stable piezoelectricity at high temperatures is attributed to enhanced electrical homogeneity and reduced conductivity.

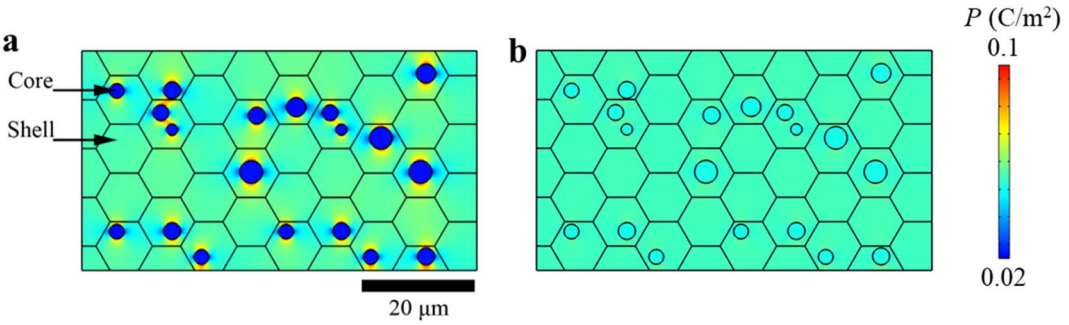


Fig. 7 The polarization distribution for the electrically heterogeneous (a) and homogeneous (b) dielectrics simulated by COMSOL Multiphysics. For the former, the conductivity of the core is much higher than the shell. For the latter, the conductivity of both is almost the same.

# 3. Conclusion

We introduce a novel metric to quantitatively assess the temperature stability of piezoelectricity, where exceptional temperature stability is characterized by a broad temperature range and high operating temperature concurrently. This metric has been validated for both commercial PZTs and lead-free piezoelectric materials. Although the temperature stability of lead-free Sm-doped BF–BT ceramics is inferior to that of commercial PZT-4 and PZT-5A, it surpasses that of commercial PZT-8. Notably, the enhanced temperature stability in the Sm-doped BF–BT ceramic, compared to its undoped counterpart, is attributed to the suppression of electrical inhomogeneity resulting from a reduction in defect concentration. This work is poised to serve as a paradigm for the design of high-temperature piezoelectrics and pave the way for the development of high-temperature electronic devices.

# 4. Materials and methods

## 4.1 Material preparation

The $0.7BiFeO_3$–$0.3Ba_{1-x}Sm_xTiO_3$ ($x$ = 0, 0.01, 0.02, 0.03, 0.04) ceramics were prepared by a conventional solid-state reaction. The raw powders, $Bi_2O_3$, $Fe_2O_3$, $BaCO_3$, $TiO_2$ and $Sm_2O_3$, were dried and then weighed according to the stoichiometric ratio. The powders were mixed by ball milling in ethanol. The dried mixture was calcined at 800 °C for 6 h and then was refined by ball milling in ethanol. The 5% PVA solution was added into the dried powder. The powders were formed into pellets by uniaxial pressing of ~200 MPa, followed by binder burn-out at 600 °C. The samples were sintered at 980–1020 °C for 3 h. All sintered ceramics were annealed at 800 °C for 2 h in an air atmosphere, followed by an air-quenching process before the temperature drops. Subsequently, the surfaces of the samples were ground. Silver electrodes were prepared by magnetron sputtering (Q150T ES Plus, Quorum Technologies), followed by annealing at 400 °C. The samples were poled under an electric field of 4.5–5 kV mm$^{-1}$ at 80–120 °C for 30 min. After aging for 24 h, the electrical properties were measured.

The commercial PZTs (PZT-5A, PZT-4 and PZT-8) are purchased from Zhuhai Jiaming Electronic Technology Co., Ltd.

## 4.2 Material characterization

The bulk densities of the ceramics were measured using a density meter (XS104, Mettler Toledo, Switzerland). The crystal structures of the powder samples were examined with X-ray diffraction (D8 advance, Bruker). The lattice parameters and phase content were analyzed with Rietveld refinement software (Topas 3.0). The morphology and grain size of the sample were observed using a scanning electron microscope (Quanta 450, FEI). To observe the ferroelectric domain, the electrodes of the poled sample were ground off and the surfaces were polished. The ferroelectric domains were identified with an atomic force microscope (Dimension Icon with ScanAsyst, Bruker) in an optimized vertical domain mode. In the measurement, a conductive probe (Asyelec.02-R2, Asylum research) is utilized. Chemical states of oxygen were detected by X-ray photoelectron spectroscopy (Axis Supra+, Kratos Analytical).

The capacitance and loss of the poled sample were tested with an inductance capacitance resistance meter (E4980A, Agilent Technologies) at temperatures of 20–600 °C with a heating rate of 3 °C min$^{-1}$. The ferroelectric polarization and electric-field induced strain were measured using a ferroelectric test system (CPE1801, PolyK Technologies) equipped with a fotonic sensor (MTI2100, MTI Instruments). The high-temperature impedance in the frequency range of $10^{-2}$ Hz to $10^{7}$ Hz was measured using a broadband impedance spectrometer (Concept 40, Novocontrol Technologies) under a small alternating voltage of 1 $V_{RMS}$, and the impedance spectra were fitted using commercial software (ZSimpWin). The piezoelectric charge coefficients at various temperatures were tested using an *in situ* quasi-static $d_{33}$ meter (TZFD-600, Harbin Julang Technology), with a heating rate of 3 °C min$^{-1}$. The impedances and phase angles of poled samples near the resonance frequency were measured using an ENA network analyzer (E5061B, Keysight).

# Conflicts of interest

There are no conflicts to declare.

# Data availability

All the data have been presented in the manuscript and supplementary information (SI). Supplementary information is available. See DOI: https://doi.org/10.1039/d5ta09690a.

# Acknowledgements

The research was supported by the National Natural Science Foundation of China (Project No. T2522031), the Hong Kong Research Grants Council (General Research Fund Project No. 16214025), and the Innovation and Technology Fund (Project No. ITS/232/24) of the Innovation and Technology Commission, the Government of the Hong Kong Special Administrative Region. We thank Prof. Dragan Damjanovic for revising the manuscript.

# References

1 G. H. Haertling, *J. Am. Ceram. Soc.*, 1999, **82**, 797–818.
2 F. Li, D. B. Lin, Z. B. Chen, Z. X. Cheng, J. L. Wang, C. C. Li, Z. Xu, Q. W. Huang, X. Z. Liao, L. Q. Chen, T. R. Shrout and S. J. Zhang, *Nat. Mater.*, 2018, **17**, 349–354.
3 X. Ren, *Nat. Mater.*, 2004, **3**, 91–94.
4 Y. Dong, K. Zou, R. Liang and Z. Zhou, *Prog. Mater. Sci.*, 2023, **132**, 101026.
5 G. Huangfu, K. Zeng, B. Wang, J. Wang, Z. Fu, F. Xu, S. Zhang, H. Luo, D. Viehland and Y. Guo, *Science*, 2022, **378**, 1125–1130.
6 J. Rödel, K. G. Webber, R. Dittmer, W. Jo, M. Kimura and D. Damjanovic, *J. Eur. Ceram. Soc.*, 2015, **35**, 1659–1681.
7 J. Wu, D. Xiao and J. Zhu, *Chem. Rev.*, 2015, **115**, 2559–2595.

 

8 S. Kim, R. Miyauchi, Y. Sato, H. Nam, I. Fujii, S. Ueno, Y. Kuroiwa and S. Wada, *Adv. Mater.*, 2023, **35**, 2208717.
9 M.-H. Zhang, C. Shen, C. Zhao, M. Dai, F.-Z. Yao, B. Wu, J. Ma, H. Nan, D. Wang, Q. Yuan, L. L. da Silva, L. Fulanović, A. Schökel, P. Liu, H. Zhang, J.-F. Li, N. Zhang, K. Wang, J. Rödel and M. Hinterstein, *Nat. Commun.*, 2022, **13**, 3434.
10 G. Wang, T. Hu, W. Zhu, Z. Lu, A. Kleppe, M. Diaz Lopez, A. Feteira, D. C. Sinclair, Z. Fu, H. Huang, D. Wang and I. M. Reaney, *Phys. Rev. Lett.*, 2023, **130**, 076801.
11 Y. Saito, H. Takao, T. Tani, T. Nonoyama, K. Takatori, T. Homma, T. Nagaya and M. Nakamura, *Nature*, 2004, **432**, 84–87.
12 M. Waqar, H. Wu, J. S. Chen, K. Yao and J. Wang, *Adv. Mater.*, 2022, **34**, 2106845.
13 J. Wu, Z. Fan, D. Xiao, J. Zhu and J. Wang, *Prog. Mater. Sci.*, 2016, **84**, 335–402.
14 J. Wu, *J. Appl. Phys.*, 2020, **127**, 190901.
15 D. Wang, G. Wang, S. Murakami, Z. Fan, A. Feteira, D. Zhou, S. Sun, Q. Zhao and I. M. Reaney, *J. Adv. Dielectr.*, 2018, **08**, 1830004.
16 Z. Shen, J. Guo, X. Gao, W. Xuan, J. Zhang, D. Wang, J. Cheng, S. Zhang and J. Chen, *J. Materiomics*, 2025, **11**, 100946.
17 H. Li, J. Zhao, Y. Li, L. Chen, X. Chen, H. Qin, H. Zhou, P. Li, J. Guo and D. Wang, *ACS Appl. Mater. Interfaces*, 2024, **16**, 9078–9087.
18 M. H. Lee, D. J. Kim, J. S. Park, S. W. Kim, T. K. Song, M.-H. Kim, W.-J. Kim, D. Do and I.-K. Jeong, *Adv. Mater.*, 2015, **27**, 6976–6982.
19 J. Chen, J. E. Daniels, J. Jian, Z. Cheng, J. Cheng, J. Wang, Q. Gu and S. Zhang, *Acta Mater.*, 2020, **197**, 1–9.
20 G. Wang, Z. Fan, S. Murakami, Z. Lu, D. A. Hall, D. C. Sinclair, A. Feteira, X. Tan, J. L. Jones, A. K. Kleppe, D. Wang and I. M. Reaney, *J. Mater. Chem. A*, 2019, **7**, 21254–21263.
21 J. Lin, F. Lv, Z. Hong, B. Liu, Y. Wu and Y. Huang, *Adv. Funct. Mater.*, 2024, **34**, 2313879.
22 W. Jia, Y. Hou, M. Zheng, Y. Xu, M. Zhu, K. Yang, H. Cheng, S. Sun and J. Xing, *IET Nanodielectr.*, 2018, **1**, 3–16.
23 W. Jia, Y. Hou, M. Zheng, Y. Xu, X. Yu, M. Zhu, K. Yang, H. Cheng, S. Sun and J. Xing, *J. Am. Ceram. Soc.*, 2018, **101**, 3468–3479.
24 American National Standard, *Ceramic Dielectric Capacitors Classes I, II, III, and IV. Part 1, Characteristics and requirements*, Electronic Components, Assemblies & Materials Association, EIA, Arlington, VA, 2002.
25 J.-S. Zhou, K. Wang, F.-Z. Yao, T. Zheng, J. Wu, D. Xiao, J. Zhu and J.-F. Li, *J. Mater. Chem. C*, 2015, **3**, 8780–8787.
26 T. Zheng, H. J. Wu, Y. Yuan, X. Lv, Q. Li, T. L. Men, C. Zhao, D. Q. Xiao, J. G. Wu, K. Wang, J. F. Li, Y. L. Gu, J. Zhu and S. J. Pennycook, *Energy Environ. Sci.*, 2017, **10**, 528–537.
27 X. D. Yan, M. P. Zheng, X. Gao, M. K. Zhu and Y. D. Hou, *Acta Mater.*, 2020, **187**, 29–40.
28 W. F. Liu and X. B. Ren, *Phys. Rev. Lett.*, 2009, **103**, 257602.
29 D. Xue, Y. Zhou, H. Bao, C. Zhou, J. Gao and X. Ren, *J. Appl. Phys.*, 2011, **109**, 054110.
30 M. Fang, S. Rajput, Z. Dai, Y. Ji, Y. Hao and X. Ren, *Acta Mater.*, 2019, **169**, 155–161.
31 C. R. Qiu, B. Wang, N. Zhang, S. J. Zhang, J. F. Liu, D. Walker, Y. Wang, H. Tian, T. R. Shrout, Z. Xu, L. Q. Chen and F. Li, *Nature*, 2020, **577**, 350–354.
32 B. Xun, A. Song, J. Yu, Y. Yin, J. F. Li and B. P. Zhang, *ACS Appl. Mater. Interfaces*, 2021, **13**, 4192–4202.
33 P. Zheng, J. L. Zhang, Y. Q. Tan and C. L. Wang, *Acta Mater.*, 2012, **60**, 5022–5030.
34 D. Ghosh, A. Sakata, J. Carter, P. A. Thomas, H. Han, J. C. Nino and J. L. Jones, *Adv. Funct. Mater.*, 2014, **24**, 885–896.
35 R. D. Shannon, *Acta Crystallogr.*, 1976, **32**, 751–767.
36 M. M. Kumar, A. Srinivas and S. V. Suryanarayana, *J. Appl. Phys.*, 2000, **87**, 855–862.
37 S. Kim, G. P. Khanal, H.-W. Nam, I. Fujii, S. Ueno, C. Moriyoshi, Y. Kuroiwa and S. Wada, *J. Appl. Phys.*, 2017, **122**, 164105.
38 Y. Nahas, A. Akbarzadeh, S. Prokhorenko, S. Prosandeev, R. Walter, I. Kornev, J. Iniguez and L. Bellaiche, *Nat. Commun.*, 2017, **8**, 15944.
39 F.-Z. Yao, K. Wang, W. Jo, K. G. Webber, T. P. Comyn, J.-X. Ding, B. Xu, L.-Q. Cheng, M.-P. Zheng, Y.-D. Hou and J.-F. Li, *Adv. Funct. Mater.*, 2016, **26**, 1217–1224.
40 D. V. Karpinsky, M. V. Silibin, S. V. Trukhanov, A. V. Trukhanov, A. L. Zhaludkevich, S. I. Latushka, D. V. Zhaludkevich, V. A. Khomchenko, D. O. Alikin, A. S. Abramov, T. Maniecki, W. Maniukiewicz, M. Wolff, V. Heitmann and A. L. Kholkin, *Nanomaterials*, 2020, **10**, 801.
41 G. Liu, S. Zhang, W. Jiang and W. Cao, *Mater. Sci. Eng. R*, 2015, **89**, 1–48.
42 M. Habib, P. Ahmad, F. Akram, I. Kebaili, A. Rahman, I. U. Din, M. Javid Iqbal, M.-H. Kim, S. Lee, M. Uddin Khandaker, H. Goo Yeo, A. Karoui and T. K. Song, *Ceram. Int.*, 2022, **48**, 26608–26617.
43 N. Hirose and A. R. West, *J. Am. Ceram. Soc.*, 1996, **79**, 1633–1641.
44 G. Wang, J. Li, X. Zhang, Z. Fan, F. Yang, A. Feteira, D. Zhou, D. C. Sinclair, T. Ma, X. Tan, D. Wang and I. M. Reaney, *Energy Environ. Sci.*, 2019, **12**, 582–588.
45 X. Guo and Z. Zhang, *Acta Mater.*, 2003, **51**, 2539–2547.
46 F. D. Morrison, D. C. Sinclair and A. R. West, *J. Am. Ceram. Soc.*, 2001, **84**, 531–538.
47 Y. Deng, J. Dai, Z. Fan, W. Yue, F. Huang, A. A. Mohamad, A. Evcin, Y. Tabak, G. Abdurakhmanov, M. Abu Abdeen and D. Wang, *Ceram. Int.*, 2025, **51**, 55067–55072.
48 O. Raymond, R. Font, N. Suarez-Almodovar, J. Portelles and J. M. Siqueiros, *J. Appl. Phys.*, 2005, **97**, 084107.
49 Z. Zhao, Y. Lv, Y. Dai and S. Zhang, *Acta Mater.*, 2020, **200**, 35–41.
50 B.-W. Xun, N. Wang, B.-P. Zhang, X.-Y. Chen, Y.-Q. Zheng, W.-S. Jin, R. Mao and K. Liang, *Ceram. Int.*, 2019, **45**, 24382–24391.